

Three-dimensional reconstruction of statistically optimal unit cells of multimodal particulate composites*

B.C. Collins², K. Matouš^{1†}and D. Rypl³

July 16, 2009

¹ Department of Aerospace and Mechanical Engineering
University of Notre Dame
Notre Dame, IN 46556, USA.

² Computational Science and Engineering
University of Illinois at Urbana-Champaign
Urbana, IL 61801, USA.

³ Department of Mechanics
Czech Technical University in Prague
Prague, 160 00, Czech Republic.

Abstract

In the current digital age, it is befitting that complex heterogeneous materials, such as solid propellants, are characterized by digital computational and/or experimental techniques. Of those, micro computer tomography (micro-CT) and advanced packing algorithms are the most popular for identifying the statistics of multimodal, random, particulate composites. In this work, we develop a procedure for the characterization and reconstruction of periodic unit cells of highly filled, multimodal, particulate composites from a packing algorithm. *Rocpack*, a particle packing software, is used to generate the solid propellant microstructures and one-, two- and three-point probability functions are used to describe their statistical morphology. However, both the experimentally scanned or computationally designed packs are usually non optimal in size and likely too big to be fully numerically resolved when complex nonlinear processes such as combustion, decohesion, matrix tearing, etc. are modeled. Thus, domain

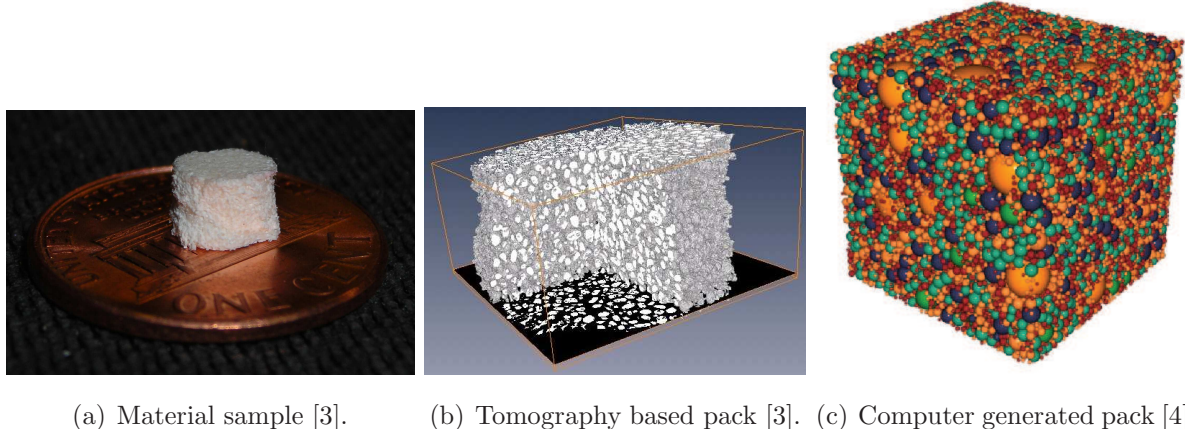
*Accepted for publication in the *International Journal for Multiscale Computational Engineering*.

†Corresponding author: kmatous@nd.edu (K. Matouš)

reduction techniques, which can reconstruct the optimal periodic unit cell, are important to narrow the problem size while preserving the statistics. The three dimensional reconstruction is carried out using a parallel Augmented Simulated Annealing algorithm. Then, the resulting cell geometries are discretized, taking into consideration the periodic layout using our master/slave approach implemented into a sophisticated meshing generator *T3D*. Final discretized geometries show only a small loss of volume fraction. Particulate systems composed of 40% and 70% volume fractions are investigated, and the unit cells are reconstructed such that the statistical correspondence to the original packs is maintained.

1 Introduction

The macroscopic properties of a random heterogeneous composite are often closely correlated to the material microstructure and the material microscale behavior [1, 2]. Conventional methods for computing the macroscopic properties of such composites often use limited information, such as the volume fraction. However, the microstructure of random heterogeneous composites is usually complicated and such limited information is not enough to be representative of a material. An example of the complicated microstructure can be seen in Figure 1, which shows a sample of a heterogeneous solid propellant along with its tomographic image [3], and the computationally generated microstructure by *Rocpack* [4].



(a) Material sample [3]. (b) Tomography based pack [3]. (c) Computer generated pack [4].

Figure 1: Typical members of the micro-CT based and the computationally generated ensemble.

The present work is focused on the characterization of random composite microstructures, primarily on highly packed systems, such as heterogeneous solid propellants. Solid propellants are composite materials made of crystalline Ammonium Perchlorate (AP) and Aluminum (Al) particles embedded in a fuel binder to increase the burning temperature and thus the thrust. Solid propellants are generally composed of particle sizes of AP and Al ranging from five to three hundred microns. This wide range of particle sizes is divided into different modes. Most industrial propellants are prepared by mixing several modes to achieve required thermo-mechanical

and combustion properties.

There are multiple methods to determine the macroscopic properties of random composites which are described above. This work is concerned with multiscale methods, where analyses are generally conducted on a representative volume element (RVE) [5, 10]. The definition imposed by Hill [1] implies that the RVE should be big enough to contain a large number of inclusions in order to account for all the possible configurations of the inclusions in a composite. Povirk [6] proposed another approach to determine the RVE. The method relies on a description of the microstructure using a certain statistical descriptor function. The RVE can then be determined by requiring the same statistical descriptor function for the RVE to match the function of the original microstructure. The second approach is adopted here.

There is a strong physical evidence that the RVE size is deeply effected by material processes. For example, Swaminathan and Ghosh show that in the presence of damage the RVE size grows rapidly [7]. In their two-dimensional investigation, the statistically equivalent RVE was reported to be thirty six times the diameter of a fiber. In three-dimensions, the effect is usually more pronounced. Experimental investigation of Liu [8] has also demonstrated that for a highly packed plastically bonded explosive, like PBX 9501, the RVE size should be large. In his study, the RVE size was reported about fifteen times the mean diameter of the crystals in the material. Thus, a detailed understanding of a material morphology and the proper makeup of the computational domain is essential.

In order to characterize the complex microstructure described above (Figure 1), statistical descriptors are used. A number of statistical descriptors are available, many of which are described in [13]. In the present study, the general n -point probability functions are used to quantify the statistics of the microstructure [14]. The n -point probability functions give the probability of simultaneously locating n points inside the matrix or the other particle phases. Due to difficulties in computation, most works focus on the first and second probability functions, disregarding the higher order statistics [22]. This paper addresses the first, second, and third order probability functions in attempt to verify whether higher order descriptors are justly discounted. Our code, *Stat3D*, computes the statistics in parallel, allowing for large domains to be quickly evaluated and higher statistical moments to be computed accurately.

Early work with n -point probability functions was performed by Corson, by manually sampling micrographs of real composite materials [15]. Here, sampling grids are used to numerically evaluate and average n -point probability functions in parallel using Message Passing Interface (MPI). For non-digitized media, Smith and Torquato [16] proposed the use of a sampling template for evaluation of two-point probability functions. This template is implemented in the current work during the calculation of the two- and three-point probability functions as well.

The reconstruction of random media using microstructural information based on a specific statistical descriptor is the primary focus of this work. In order to address this issue, Yeong and Torquato [17] proposed a method of reconstruction of random media based on two-point

probability functions using Simulated Annealing (SA). Bochenek and Pyrz [18] also used the Simulated Annealing procedure in conjunction with the pair correlation function and the stress interaction parameter for a reconstructed unit cell. However, a simple pair correlation function does not represent the disparate particle modes, and thus, it restricts the probability spectrum to be optimized. Another approach introduced by Sundararaghavan and Zabaras [19] employs the support vector machines for three-dimensional reconstruction of microstructures.

The present paper is an extension on our earlier work [20], where two-dimensional periodic cells of multimodal fibrous composites were reconstructed, emphasizing the discrete nature of the whole probability spectrum. Here, we advance this methodology to three dimensions and apply it to the reconstruction of multimodal particulate composites, where the full second-order probability spectrum is optimized. Inspiration is also obtained from [21] and [22], where a Periodic Unit Cell (PUC) was reconstructed for a two-phase fibrous composite using two-point probability functions, a lineal path function and a second-order intensity function. Our code, *Recon3D*, reconstructs the unit cell in parallel, preserving the end-to-end parallelism and allowing for the optimal computational domain to be generated quickly.

Finally, we also present the finite element discretization of our cells. In the present work, periodic boundary conditions are enforced and directly embedded in geometry description using our meshing approach [9] based on the *T3D* meshing tool [11]. Periodic boundary conditions are extensively used in computational studies due to their simplicity, reasonable physical relevance and their deep mathematical foundation [12]. This allows the microstructure to be replaced by an infinite domain, and thus, the complicated microstructure can be replaced by a periodic unit cell. This PUC contains many less inclusions than the original microstructure, but still contains important statistical information, allowing for an accurate material response to be captured by the model.

2 Morphology of Microstructure

It is well established that the effective properties of a heterogeneous material are dependent both on the properties of each phase and the microstructural layout [1, 23]. Moreover, the effective properties of a material are not simply relations involving only the volume fraction of each phase, but are also dependent on the complex interactions between phases, which is determined by the microstructural information [13, 24].

2.1 n-point Probability Functions

The tools that are necessary to characterize the morphology of a heterogeneous composite are described in this section. Specifically, the statistical descriptors known as the one-, two- and three-point probability functions that characterize the random microstructure morphology are described for completeness of the presentation. In order to characterize the statistical description

of a material, an indicator function, or the characteristic function $\chi_r(\mathbf{x}, \omega)$ is defined:

$$\chi_r(\mathbf{x}, \omega) = \begin{cases} 1 & \mathbf{x} \in D_r(\omega) \\ 0 & \text{otherwise,} \end{cases} \quad (1)$$

where \mathbf{x} is a random point thrown into the material, ω is a particular ensemble member and D_r represents the domain occupied by the r -th phase. This definition allows for the formulation of the n -point probability function, S_{r_1, r_2, \dots, r_n} , which gives the probability of finding phases r_1, r_2, \dots, r_n simultaneously at points x_1, x_2, \dots, x_n :

$$S_{r_1, \dots, r_n}(\mathbf{x}_1, \dots, \mathbf{x}_n) = \overline{\chi_{r_1}(\mathbf{x}_1) \dots \chi_{r_n}(\mathbf{x}_n)}, \quad (2)$$

where the overbar indicates the ensemble average:

$$\overline{\chi_r(\mathbf{x})} = \int_{\mathcal{S}} \chi_r(\mathbf{x}, \omega) p(\omega) d\omega. \quad (3)$$

Here $p(\omega)$ denotes the probability density of ω in the ensemble space \mathcal{S} . An ensemble is defined to be a large collection of microstructure samples that are different in their microscopic details, but identical in the macroscopic sense.

The probability functions that are used hereafter are the one-point, two-point, and three-point probability functions, which are shown as

$$\begin{aligned} S_r(\mathbf{x}) &= \overline{\chi_r(\mathbf{x})}, \\ S_{rs}(\mathbf{x}, \mathbf{x}') &= \overline{\chi_r(\mathbf{x}) \chi_s(\mathbf{x}')}, \\ S_{rsq}(\mathbf{x}, \mathbf{x}', \mathbf{x}'') &= \overline{\chi_r(\mathbf{x}) \chi_s(\mathbf{x}') \chi_q(\mathbf{x}'')}. \end{aligned} \quad (4)$$

Evaluation of probability functions is expensive, but can be simplified if the microstructure of the material under consideration is ergodic, statistically isotropic, and homogeneous [25]. Ergodicity, statistical isotropy and homogeneity reduce the evaluation costs, since they lead to ensemble member independence, directional independence and translation independence, respectively. For a random heterogeneous material that meets these criteria, the one-, two-, and three-point probability functions can be reduced to

$$\begin{aligned} S_r(\mathbf{x}) &= S_r = c_r, \\ S_{rs}(\mathbf{x}, \mathbf{x}') &= S_{rs}(\mathbf{x} - \mathbf{x}') = S_{rs}(\|\mathbf{x} - \mathbf{x}'\|), \\ S_{rsq}(\mathbf{x}, \mathbf{x}', \mathbf{x}'') &= S_{rsq}(\mathbf{x} - \mathbf{x}', \mathbf{x} - \mathbf{x}'') = S_{rs}(\|\mathbf{x} - \mathbf{x}'\|, \|\mathbf{x} - \mathbf{x}''\|), \end{aligned} \quad (5)$$

where c_r represents the volume fraction of phase r in the composite, $\|\mathbf{x} - \mathbf{x}'\|$ represents the distance between points \mathbf{x} and \mathbf{x}' , and $\|\mathbf{x} - \mathbf{x}''\|$ represents the distance between points \mathbf{x} and \mathbf{x}'' . Further properties of the two-point probability functions yield

$$\begin{aligned} S_{rr}(0) &= S_r = c_r, \\ S_{rs}(\|\mathbf{x} - \mathbf{x}'\|) &= S_r(\mathbf{x}) S_s(\mathbf{x}') = c_r c_s, \end{aligned} \quad (6)$$

provided that $\|\mathbf{x} - \mathbf{x}'\|$ is sufficiently large. Likewise, properties for the three-point probability functions are

$$\begin{aligned} S_{rrr}(0) &= S_r = c_r, \\ S_{rrq}(\|\mathbf{x} - \mathbf{x}'\|) &= S_{rrq}(0, \|\mathbf{x} - \mathbf{x}'\|) = S_{rq}(\|\mathbf{x} - \mathbf{x}'\|), \\ S_{rsq}(\|\mathbf{y} - \mathbf{y}'\|, \|\mathbf{y} - \mathbf{y}''\|) &= S_r(\mathbf{y}) S_s(\mathbf{y}') S_q(\mathbf{y}'') = c_r c_s c_q, \end{aligned} \quad (7)$$

provided that $\|\mathbf{y} - \mathbf{y}'\|$ and $\|\mathbf{y} - \mathbf{y}''\|$ are sufficiently large.

2.2 Numerical Sampling

The n -point probability functions for a given microstructure are typically highly complex, and therefore finding a closed form representation of these functions would be unlikely. Instead, the probability space can be discretized and the probability functions can be numerically sampled via the Monte-Carlo method. In addition, a particular sampling template can be used in order to increase the sampling efficiency and take advantage of cases where the microstructure may be statistically isotropic [16].

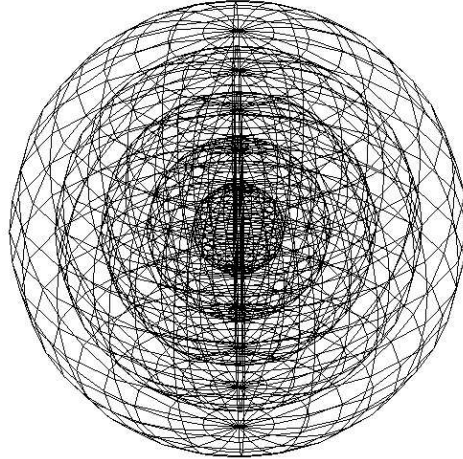


Figure 2: Three-dimensional sampling template.

In this work, a spherical sampling template is used to compute the discrete probability functions of a continuous heterogeneous material (Fig. 2). Details on the parallel implementation are discussed in section 5.3. It should be noted that the accuracy of the evaluated statistics depends both on the number of random samples taken and the template resolution, therefore a convergence study is performed for every material type (given pack) to assure numerically converged solutions.

3 Reconstruction of Periodic Unit Cells

This section is dedicated to the reconstruction of a three-dimensional periodic unit cell of general particulate composites. As mentioned in section 1, the microstructure of the real material may be obtained via tomographic data or by a packing code such as *Rocpack* [4, 24]. In this section, the PUC is determined such that it has similar statistical properties as the original microstructure (pack). In order to ensure similarity between the original microstructure and the PUC, an objective function is constructed, which incorporates the statistical descriptors discussed in section 2.

There are two main steps to the reconstruction of the PUC: finding the optimal PUC dimensions and finding the optimal particle locations within the PUC, subjected to the constraint that particles do not overlap. Finding the optimal dimensions of the PUC can be solved with a closed-form solution, but finding the optimal particle positions is a more complex process. Since it requires solving the minimization problem on a multimodal function, use of a stochastic algorithm is preferable to gradient search methods [21]. A variety of stochastic algorithms are available, with an *Augmented Simulated Annealing* being chosen for the current work.

3.1 Objective Function and Problem Definition

Once the statistics of a heterogeneous microstructure are determined, a PUC of an optimal size can be reconstructed. In the present study, a PUC is considered to be representative of the original microstructure if its geometric descriptors, or n -point probability functions, are similar to those of the actual material (pack or tomographic image). In particular, the one- and two-point probability functions are optimized. These optimization conditions are described as follows:

(a) The volume fraction of each phase in the PUC must be similar to that of the microstructure. The length scale of the PUC, H_{in} , is obtained by examining where the two-point probability functions saturate and therefore become statistically independent. Based on this initial guess, the corresponding volume fractions and particle radii, we compute the number of particles N_i needed in each bin i . Note that only a whole particle can be added into a cell introducing an error between the corresponding volume fraction values. Thus, for this given number of particles N_i of phase i , volume fractions c_i and the particle radius r_i the PUC dimension H is found such that the differences in the volume fractions are minimized using the following objective function:

$$G(H) = \sqrt{\sum_{i=1}^{n_p} \left(c_i - \frac{4N_i\pi r_i^3}{3H^3} \right)^2}, \quad (8)$$

where n_p is the number of particle phases in the composite. This optimization problem can be

solved analytically to get the optimal dimensions of the PUC to be:

$$\frac{dG}{dH} = 0 \quad \Rightarrow \quad H = \left(\frac{4\pi \sum_{i=1}^{n_p} N_i^2 r_i^6}{3 \sum_{i=1}^{n_p} c_i N_i r_i^3} \right)^{\frac{1}{3}}. \quad (9)$$

This optimization procedure on the one-point probability functions is performed in order to ensure that the volume fractions between the PUC and the original microstructure are similar.

(b) After determining the optimal length scale of the PUC using Equation (9), and therefore optimizing its one-point probability functions, the two-point probability functions of the PUC are optimized. This is done by finding the optimal positions of the particle centers by minimizing the following objective function based on the two-point probability distributions:

$$F(\mathbf{x}_N) = \sum_{r=1}^m \sum_{s=1}^m \|S_{rs}^{orig} - S_{rs}\|_{L_2} = \sum_{r=1}^m \sum_{s=1}^m \sqrt{\int_0^H (S_{rs}^{orig} - S_{rs})^2 dr}, \quad (10)$$

where $\mathbf{x}_N = \{x_1, y_1, z_1, \dots, x_N, y_N, z_N\}^T$ is the vector of the positions of particle centers, x_i , y_i , and z_i correspond to the x , y , and z coordinates of the i -th particle, respectively, m is the total number of phases in the composite ($m = n_p + 1$), S_{rs}^{orig} are the two-point probability functions computed for the original microstructure and S_{rs} are the two-point probability functions computed for the PUC. Note that discrete L_2 norm is used in the numerical implementation.

Since the objective function in Equation (10) does not contain any information on the overlap of particles inside the PUC, a constraint restricting the overlap of particles is added to ensure the solution feasibility. Thus, the solution vector \mathbf{x}_N should comply with

$$\sqrt{(x_i - x_j)^2 + (y_i - y_j)^2 + (z_i - z_j)^2} \geq r_i + r_j, \quad \forall i = 1, \dots, N-1, \quad j = i+1, \dots, N, \quad (11)$$

where N is the total number of particles, and r_i and r_j are the radii of i -th and j -th particles, respectively. Instead of solving the minimization problem with a constraint, the constrained optimization problem is changed into an unconstrained optimization problem with a penalty:

$$\min (F(\mathbf{x}_N) + \gamma p(\mathbf{x}_N)), \quad (12)$$

where γ is a penalty coefficient, equal to 1 in the present work, and p is a penalty function. This penalty function is based on a particle overlap, and is defined below.

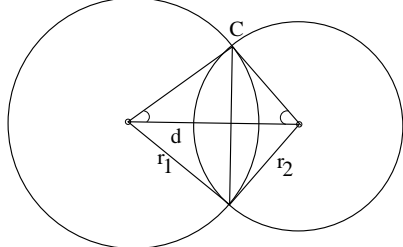
Based on the distance between the centers of a pair of particles, the overlap is divided into two classifications: partial and complete overlap. Two particles are considered to be partially overlapped if the distance between the centers is less than the sum of the radii. They are considered to be completely overlapped if the distance between the centers is less than either of the radii of the particles. This is shown graphically in Figure 3(a). Let the number of occurrences of partial overlap be denoted as N_p and the number of occurrences of complete overlap be denoted as N_c . The amount of overlap in a potential solution is described by the

parameter η as

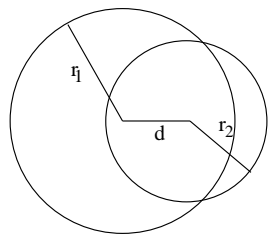
$$\eta = \begin{cases} \frac{2}{N_p} \sum_{i=1}^N \sum_{j=i}^N \frac{V_{overlap}}{(V_i + V_j)} & N_c = 0 \\ \frac{2}{N_p} \sum_{i=1}^N \sum_{j=i}^N \frac{V_{overlap}}{(V_i + V_j)} + 0.5 & N_c > 0. \end{cases} \quad (13)$$

If no instance of complete overlap occurs within the PUC (i.e., $N_c = 0$), the penalty parameter

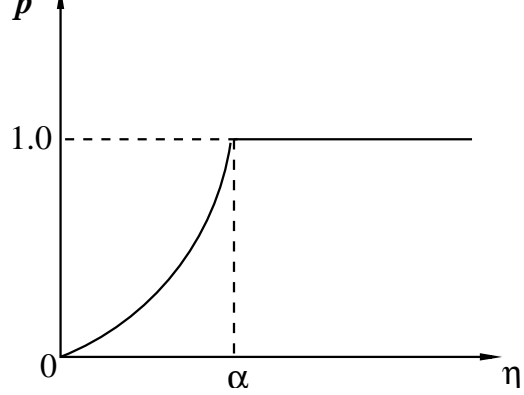
Partial overlap



Complete overlap



(a)



(b)

Figure 3: (a) Two types of overlap encountered. (b) Penalty function used.

is simply a global mean of the ratio of the volume of overlap to the mean volume of a pair of particles. The limiting case of this expression occurs when a smaller particle center is on the circumference of a larger particle. Since a complete overlap is a highly undesirable and infeasible situation, it is penalized heavily. In order to treat this scenario, 0.5 is automatically added to the overlap parameter η when there is a case of complete overlap that is encountered, so that the value of η lies within 0 and 1.

Based on the amount of overlap given by the parameter η , a constraint function, also known as a penalty function, is established as shown in Figure 3(b). The formulation of the constraint function is based on a similar one used in [26] and follows a simple power law,

$$p = \begin{cases} 0 & \eta = 0 \\ \left(\frac{\eta}{\alpha}\right)^\beta & 0 < \eta < \alpha \\ 1.0 & \eta \geq \alpha \end{cases} \quad (14)$$

where α is the upper cutoff of overlap above which $p = 1$ and β is the exponent of the penalty function in the range $0 \leq \eta \leq \alpha$.

Combining the objective function described by Equation (10) and the constraint function in Equation (14), the overall objective function, or the fitness function, is defined to be

$$f = \frac{\sum_{r=1}^m \sum_{s=1}^m \|S_{rs}^{orig} - S_{rs}\|_{L_2}}{\max_{P_0} \sum_{r=1}^m \sum_{s=1}^m \|S_{rs}^{orig} - S_{rs}\|_{L_2}} + p, \quad (15)$$

where $\max_{P_0} \sum_{r=1}^m \sum_{s=1}^m \|S_{rs}^{orig} - S_{rs}\|_{L_2}$ represents the value of the objective function of the worst individual of the starting population P_0 . The value of f always lies between 0 and 2.

3.2 Genetic Algorithm

The fitness function in Equation (15) is multimodal and contains a number of local minima. Therefore, an optimization using the conventional gradient-based methods is not suitable for this scenario. In order to address this issue, stochastic optimization methods based on the principle of evolution, such as genetic algorithms (GA) and simulated annealing (SA), are used to solve this minimization. These methods have been previously used efficiently to solve such complex optimization problems [21, 20]. In the present work, the parallel *Augmented Simulated Annealing (AUSA)* technique, which effectively exploits the essentials of GA in combination with SA, is employed to minimize the overall objective function. This algorithm is identical to that used in [20] and [26]. More information about genetic algorithms can also be found in [27].

3.3 Mass-Spring Operator

It has been observed in [20] that although the penalty parameter works to reduce overlap over time, many generations are needed for packs containing a high volume fraction. In order to reduce the computational time necessary for the optimization, a problem specific mass-spring dynamic mutation operator is employed [20]. In this work, we extend this operator to three dimensions and describe it hereafter for clarity of the presentation.

For a pair of overlapping particles, a stiff repulsive spring is introduced to push the particles away from each other and for a pair of non-overlapping particles, a soft attractive spring is introduced to keep particles close together, such that the statistics are not altered substantially by the new operator. It is assumed that the mass of the particle is directly proportional to its volume, and that the force-displacement relation for the springs is linear, with spring stiffnesses of κ or $\bar{\kappa}$ for repulsive or attractive springs, respectively, as shown in Figure 4(a). The separation, d_{ij} , between the particles i and j is computed simply as

$$d_{ij} = \|\boldsymbol{x}_i - \boldsymbol{x}_j\| - (r_i + r_j), \quad (16)$$

where \boldsymbol{x}_i and r_i are the position vectors of the center and radius of particle i , respectively.

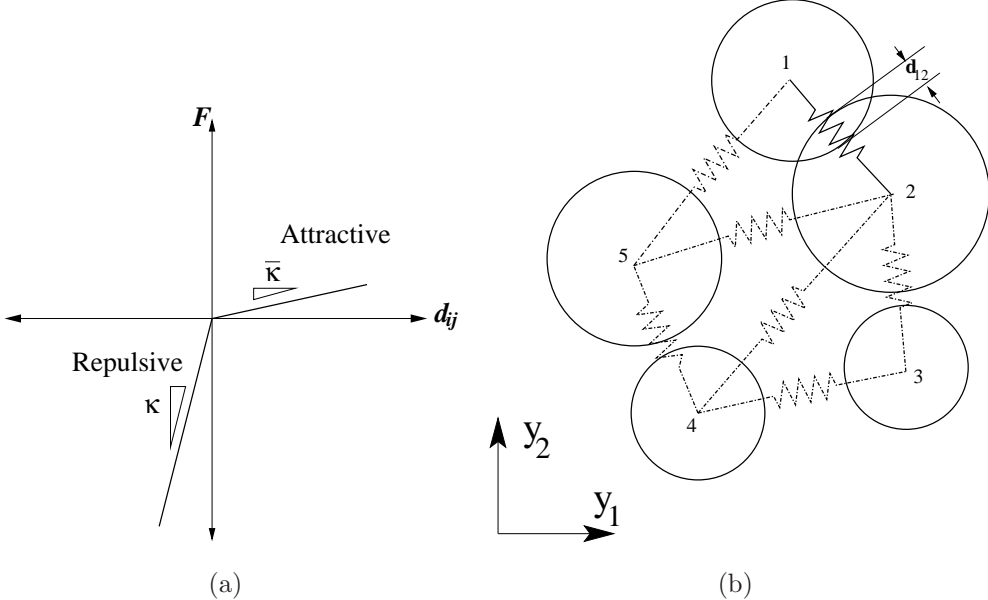


Figure 4: (a) Force-displacement (spring) relation. (b) Delaunay triangulation and position of springs in a potential cell. Symbol d_{ij} denotes the separation between particles i and j , and symbols κ and $\bar{\kappa}$ represent repulsive and attractive spring constants, respectively.

The placement of springs in a potential PUC, for two-dimensional pack, is shown schematically in Figure 4(b). First, a three-dimensional Delaunay triangulation is created from the set of particle centers using *DeWall* [28]. Then, particles sharing a tetrahedron are identified as neighbors and only neighbors interact through springs. For example in Figure 4(b), particles 1 and 2 are neighbors, while particles 1 and 4 are not. Overlapping neighbors interact through a stiff repulsive spring, as shown by solid lines in Figure 4(b), while the soft attractive springs between non-overlapping neighbors are shown in broken lines. Based on the standard spring dynamics, we construct the equation of motion as follows:

$$\mathbf{M}\ddot{\mathbf{u}} + \mathbf{K}\mathbf{u} = \mathbf{F}|_{t=0}, \quad (17)$$

where \mathbf{u} is the displacement vector, \mathbf{M} is the diagonal mass matrix, \mathbf{K} represents the global stiffness matrix and $\mathbf{F}|_{t=0} = \mathbf{K}\mathbf{y}_0$. The initial displacement conditions on \mathbf{u} are zero and an initial vector \mathbf{y}_0 , containing the starting overlap, reads

$$\mathbf{y}_0 = \frac{1}{2} \left\{ \sum_{i=2}^{\bar{N}_1} \mathbf{d}_{1i}, \sum_{\substack{i=1 \\ i \neq 2}}^{\bar{N}_2} \mathbf{d}_{2i}, \dots, \sum_{\substack{i=1 \\ i \neq N}}^{\bar{N}_N} \mathbf{d}_{Ni} \right\}^T \quad (18)$$

where N denotes the number of particles and \bar{N}_i represents the number of neighbors for i -th particle. The vector \mathbf{d}_{ij} is computed as

$$\mathbf{d}_{ij} = \left\{ \frac{\mathbf{x}_i - \mathbf{x}_j}{\|\mathbf{x}_i - \mathbf{x}_j\|} \right\}^T, \quad (19)$$

where \boldsymbol{x} is the particle location. The global stiffness and mass matrices \mathbf{K} and \mathbf{M} are constructed from their standard element counterparts by the usual assembly procedure.

The standard implicit Newmark predictor-corrector scheme is used for the time integration of Equation (17) because of its stability and simple implementation [29]. The SuperLU library is utilized for the LU decomposition [30]. The numerical integration is carried out until the overlap inside a potential PUC goes to zero or a prescribed number of time-steps is reached. In order to prevent particles from changing periodic boundary conditions during the run, and therefore requiring a new triangulation, the pack size is treated to be larger than the PUC. This creates a periodic layer of particles surrounding the PUC, acting as a buffer, which restricts a change in particle boundary conditions. In the current study, a buffer size equivalent to the diameter of the largest particle is used. This mutation operator is applied to those population members having only a partial overlap, and is activated with a small probability of 0.05.

4 Computational Geometry and Meshing

Once the reconstruction stage is completed and the geometric model is created, the material constants of the microstructure can be evaluated. It is infeasible to obtain a closed-form solution for the complicated unit cell makeup, so it is instead discretized for subsequent numerical analysis (by the finite element method, for example). In the current study, the cell is discretized into finite elements, where the periodic mesh boundary is taken into account. Here we use our master-slave approach as proposed in [9] and extend it to three-dimensions.

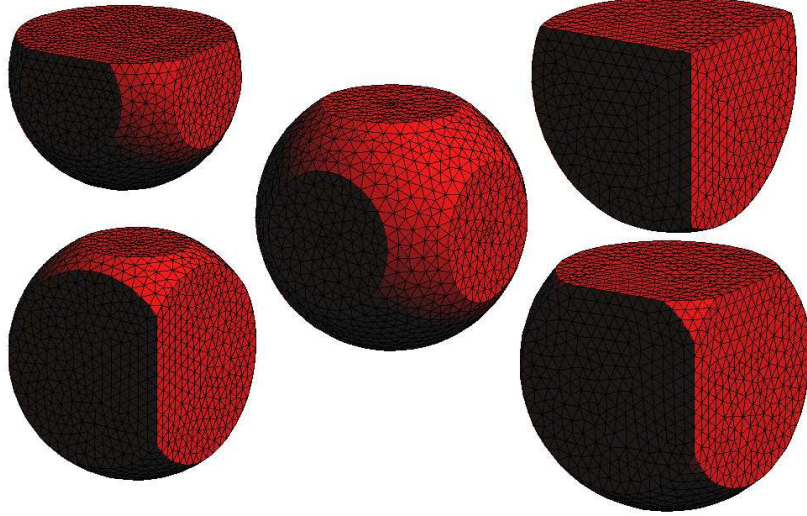


Figure 5: Various meshes of cut particles.

In order to deal with the issues described above, as well as to convert the geometrical representation into the Bézier representation needed by the meshing tool, a preprocesssing algorithm was developed. This algorithm shrinks particles in contact with other particles and/or

the reference box, computes refinement parameters for a non-uniform meshing, and constructs Bézier representations of particles both completely contained in the PUC and split by the reference box. Then, the periodic mesh is created using the software *T3D* developed by D. Rypl [11]. *T3D* is based on an advancing front technique and can mesh complex two-dimensional and three-dimensional domains into triangular and tetrahedral meshes of a high quality. An array of different potential configurations is shown in Figure 5.

4.1 Periodic meshing - Master/Slave approach

Since the identical meshes can not be obtained by an advancing front technique due to the round-off errors and mesh density control, we adopt here the master/slave model. The mirror master surface is discretized in the standard way using the advancing front technique [32]. Next, we create nodes on the mirror slave surface with the parametric coordinates as their counterparts on the mirror master (Figure 6). Mapping of the geometry of the mirror slave surface is used to

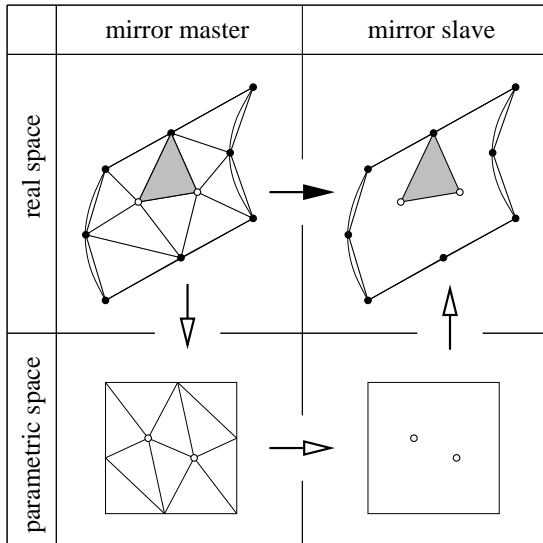


Figure 6: Mirroring of the surface mesh. The arrows visualize the flow of information to create nodes (empty arrows) and to form elements (full arrows) on the mirror slave surface.

describe their real coordinates. We use pointer arithmetics to map individual geometric entities. Each of the nodes on the mirror master surface temporarily stores a pointer to its counterpart on the mirror slave surface. Similar pointers are also established on curves bounding the mirror master surface. To create the final periodic mesh, we traverse the elements on the mirror master surface and create for each of them a new element on the mirror slave surface using the nodes being stored as pointers (Figure 6). These pointers are discarded once all the elements on a particular mirror slave have been constructed. In this way, topologically identical meshes of the same geometry are produced for all pairs of mirrored surfaces. Note that the discretization of boundary curves of mirrored surfaces, which actually precedes the surface discretization, is

performed in a similar manner. However, the mirroring of appropriate pairs of curves (derived from the mirroring of opposite surfaces) is performed automatically by *T3D*.

A similar meshing strategy for PUCs was employed by Wentorf *et al.* [31]. However, in our work the discretization is performed directly in the real space and the parametric space is used only for the mirroring of nodes. This concept avoids the demanding generation of anisotropic meshes in the parametric space, where distortion and stretching induced by the mapping may generally occur.

4.2 Particle Shrinking

Although the output from the reconstruction algorithm described in section 3 is geometrically very simple, it is directly unsuitable to be used in a numerical framework as contacting particles would lead to singularities. In order to prevent such occurrences, two particles (or a particle and the bounding box) that are closer in proximity than some user-defined parameter are shrunk until they meet the user defined tolerance.

The separation distance between particles i and j is computed as

$$\delta_{ij} = \|\mathbf{Y}_i - \mathbf{Y}_j\| - (r_i + r_j), \quad (20)$$

where \mathbf{Y} corresponds to particle location. Whenever δ_{ij} is less than a user defined minimum separation between the surfaces of adjacent particles, λ , the radii of the corresponding particles are modified such that

$$\begin{aligned} r_i^{new} &= r_i - (\lambda - \delta_{ij}) \frac{r_i}{r_i + r_j}, \\ r_j^{new} &= r_j - (\lambda - \delta_{ij}) \frac{r_j}{r_i + r_j}. \end{aligned} \quad (21)$$

4.3 Mesh Refinement

In addition to the particle contact, the existence of nearly touching particles pose some important challenges in the finite element discretization, because very small elements need to be used in those regions in order to capture the underlying physics. To address this issue, spatially dependent refinement factors are added between geometric objects that are within close proximity of each other. The refinement factor modifies the element size and is given by

$$\sigma_{ij} = \begin{cases} 0.1 + \frac{0.9}{\varepsilon - \lambda}(\delta_{ij} - \lambda) & \text{if } \lambda \leq \delta_{ij} \leq \varepsilon, \\ 1.0 & \text{if } \delta_{ij} \geq \varepsilon, \end{cases} \quad (22)$$

where ε is the user-defined maximum distance to be influenced by refinement. Since the resulting mesh depends on the parameters ε , λ , and the default element size h , they must be chosen carefully with some numerical experience.

5 Numerical Examples

This section is devoted to the discussion of the results of the statistical descriptors, optimization procedures, and PUC meshing presented in sections 2, 3, and 4. We also report on the parallel scalability of our framework.

5.1 Trimodal Pack with 40% Volume Fraction

In the task of reconstructing a periodic unit cell, a 40% pack is chosen as a starting point (Figure 7(a)). This three-dimensional pack contains 50000 trimodal particles with a particle volume fraction of 40% and an edge length of 3000 μm . The largest particle has a diameter of 200 μm with a volume fraction of 20% (mode 1), the medium particle has a diameter of 100 μm with a volume fraction of 10% (mode 2), and the smallest particle has a diameter of 50 μm with a volume fraction of 10% (mode 3). It was determined numerically that the pack is statistically isotropic and homogeneous [33].

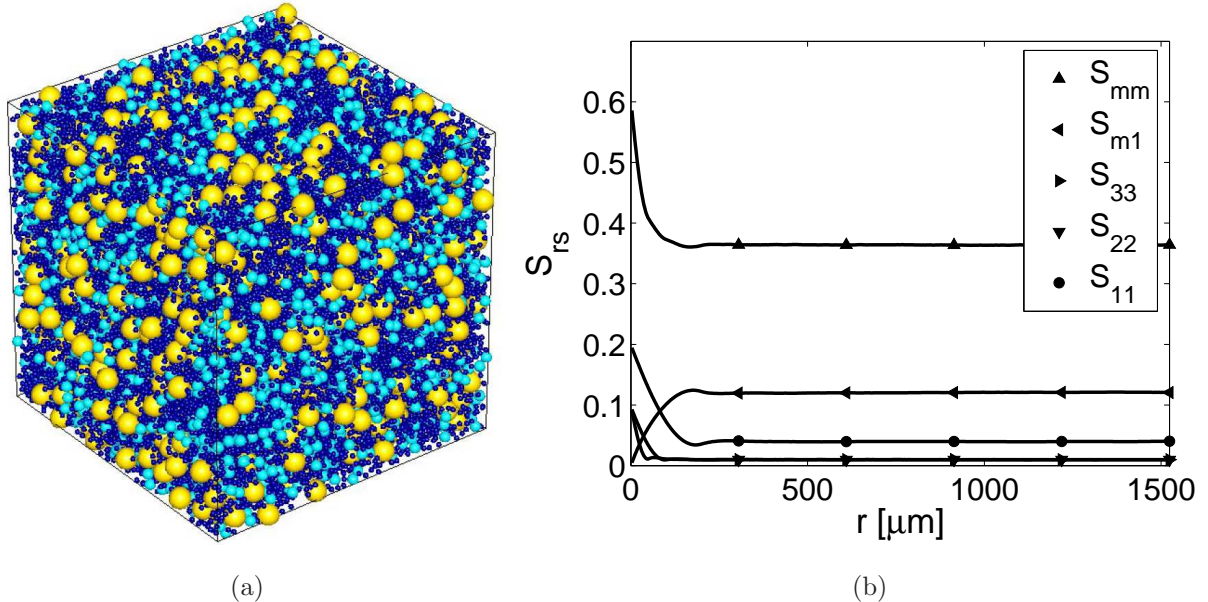


Figure 7: (a) 40% trimodal particle pack containing 50000 particles. (b) Selected two-point probability functions for the 40% pack.

The optimal radial spacing was determined to be 3 μm , and the optimal number of template throws was calibrated to be 4000 (optimal parameters were determined by a convergence study). The two-point probability functions for the pack can be seen in Figure 7(b). The initial size of the PUC, H_{in} , for this problem is chosen to be 600 μm . Using Equation (9), the optimal size of the PUC is determined to be $H = 596.6 \mu\text{m}$.

The parallel AUSA algorithm described in section 3.2 is then used to reconstruct a periodic unit cell. All the AUSA runs consisted of a population, P_0 , of 512 individuals and 16 individuals in the mating pool, M_t . During the initialization of the genetic algorithm, 50% of the individuals

are generated completely randomly and 50% of the individuals are generated using ballistic deposition, only allowing a certain degree of overlap. Table 1 lists the values used for the GA and AUSA parameters employed in the present study. The simulation is stopped when the maximum number of iterations is reached, $it_{max} = 10000$, or the best individual is not improved for 300 generations. The genetic algorithm was run five times on 128 processors on Turing computer at the University of Illinois.

The results from the minimization process can be observed in Table 2, which depicts the initial and final values of the objective function, the number of iterations needed for convergence, and the value of overall overlap $\tilde{\eta}$ ($\tilde{\eta}$ is simply defined as V_o/V_p , where V_o is a volume of overlap and V_p denotes a volume of the particles). It should be noted that the overlap is completely removed in each of the five runs. The improvement of the raw fitness of the best individual ranged from 92.7% to 96.3% over the duration of the runs.

Figure 8 shows the comparison of the mean two-point probability functions of the five reconstructed PUCs and the original pack. The error bars indicate the spread in the evaluation of the two-point probability functions in the five original packs, as well as the numerical error associated with the optimal sampling parameters. It can be observed that a very good agreement between the statistics of the pack and cell has been obtained.

One of the five reconstructed unit cells can be seen in Figure 9 together with the initial pack for visual comparison. After reconstruction, each of the periodic unit cells contain 381 particles, which is a large reduction in size compared to the original 50000 particle pack.

Due to the costly evaluation of the three-point probability functions (Figures 10-12), they are not included in the current optimization procedure. Instead, the three-point probability functions of the original pack are compared to the reconstructed unit cell. The pack and the reconstructed cell were sampled with 50000 template throws, and their respective S_{311} probability functions are shown in Figures 11 and 12.

Please note that statistical isotropy was assumed in computing the third-order statistics,

Description	Parameter	Value
Population size	P_t	512
Mating Pool size	M_t	16
Probability of mutation, crossover, dynamic mutation	$p_{mut}, p_{cro}, p_{dyn}$	0.7, 0.3, 0.1
Minimum - Maximum annealing temperature	T_{min}, T_{max}	1.5E-6, 0.05
Ratio of cooling	T_{mult}	0.999
Shape parameter for non-uniform mutation	b	2.0
Penalty function parameters	α, β	0.3, 1.0

Table 1: Parameters used in the implementation of the AUSA algorithm. See [20] and [33] for details on individual parameters.

Pack #	Raw Fitness F (Eq. 10)						# of iter.	Overall overlap ($\tilde{\eta}$)		
	Before GA			After GA						
	Min	Mean	Max	Min	Mean	Max				
Run 1	9.826	30.160	40.733	0.385	0.564	1.046	1224	0.0000		
Run 2	9.465	30.327	40.798	0.361	0.554	0.980	900	0.0000		
Run 3	9.302	23.088	40.732	0.422	0.633	1.570	521	0.0000		
Run 4	9.404	30.182	40.727	0.345	0.558	1.642	430	0.0000		
Run 5	9.279	30.270	40.752	0.414	0.678	1.347	950	0.0000		

Table 2: Final objective function values, number of iterations needed for convergence and overall overlap for the 40% pack.

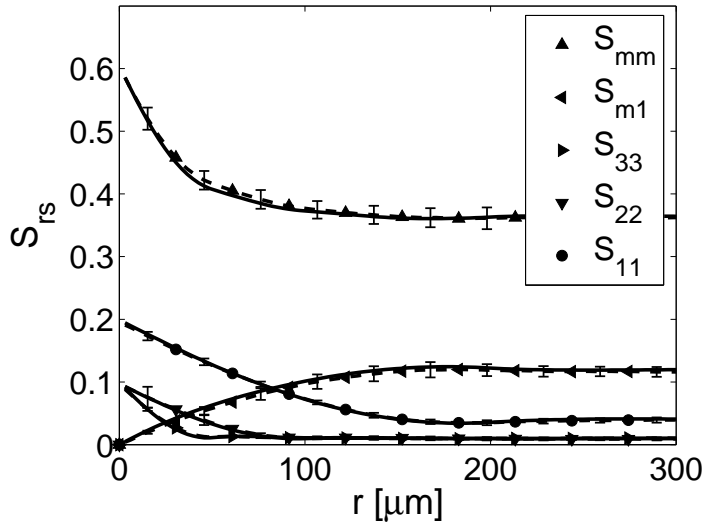
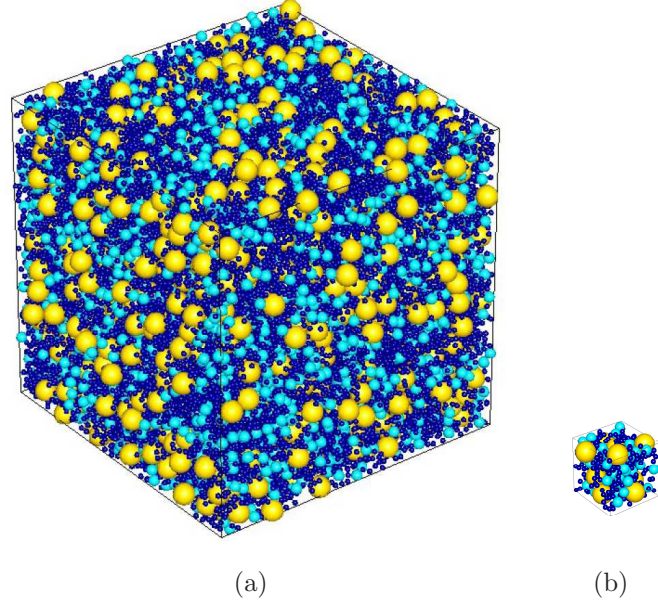


Figure 8: Comparison of the selected two-point probability functions of the original pack (solid line) and the reconstructed PUC (dashed line) for the 40% pack.

except for planar interactions. We average all possible orientations of two randomly generated vectors except its in-plane correlations as shown in Figure 10. Thus, seventh dimensional space of $S(\mathbf{x}, \mathbf{x}', \mathbf{x}'')$ is reduced to forth dimensional $S(\|\mathbf{x} - \mathbf{x}'\|, \|\mathbf{x} - \mathbf{x}''\|, \theta)$, which is possible to visualize (Eq. (5), Figure 11). When two random directions coincide $r_1 \equiv r_2$ for $\theta = 0^\circ$, the S_{rsq} goes to S_{rs} . However, physically more interesting situation occurs when a small particle sits between two big ones, $\theta = 180^\circ$, and the probability of such arrangement is $\approx 1.5\%$, (Figure 11(c)).

The S_{311} probability function was selected for evaluation, as it informs on the probability of finding a small particle between two large ones. Such a configuration leads to stress concentrations and a potential debonding. The differences between S_{311} of the pack and the cell (Figs. 11 and 12) are shown in Figure 13. It can be observed that there are noticeable differences be-



(a)

(b)

Figure 9: (a) Initial pack consists of 50000 particles. (b) Statistically identical unit cell consists of 381 particles.

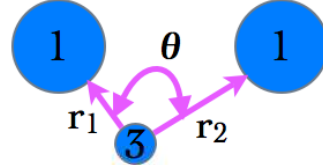


Figure 10: Concept of the three-point probability function evaluation.

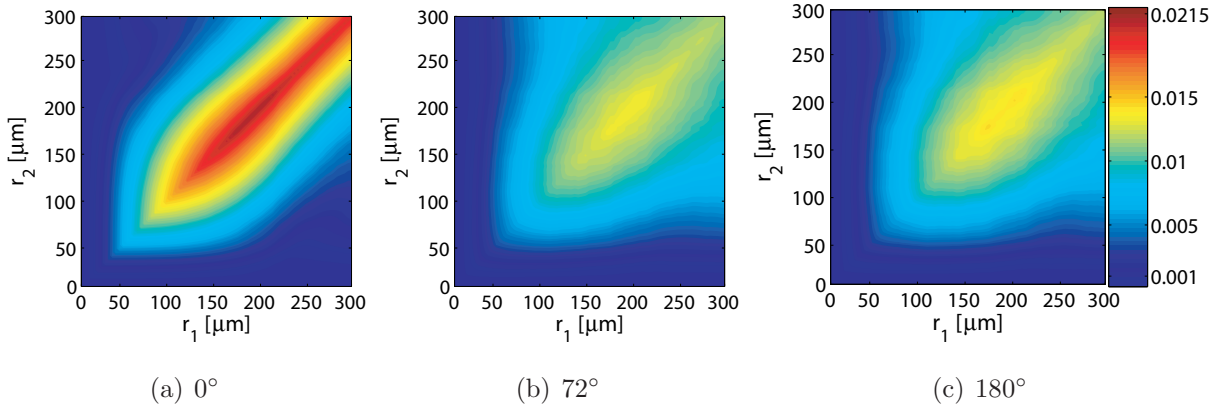


Figure 11: Various samples of the 3-point probability function S_{311} on the original pack.

tween the statistics of the original pack and its reconstructed cell, even though the second-order probabilities are in excellent agreement (Fig. 8). These differences indicate that optimization of the three-point probability functions may be a necessary future step.

The cell reconstructed from run four was chosen for meshing, as it had the lowest raw fitness

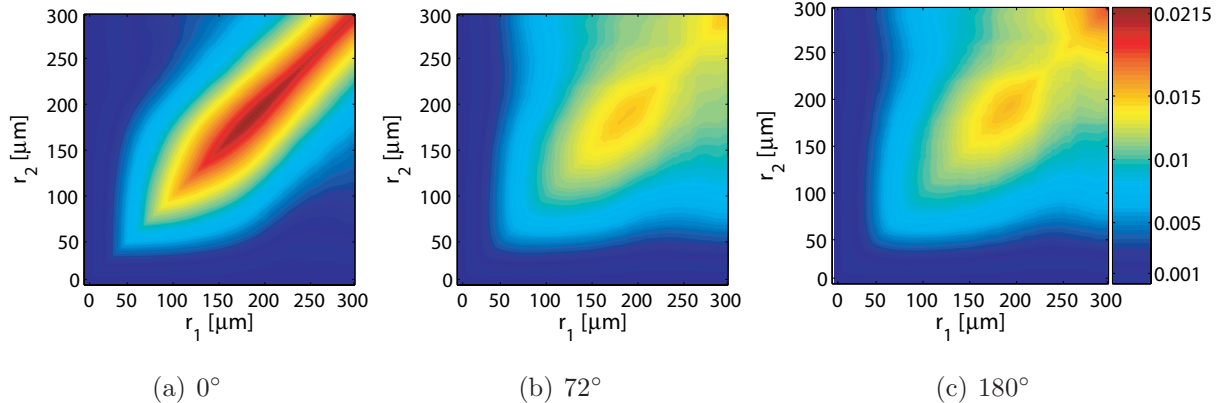


Figure 12: Various samples of the 3-point probability function S_{311} on a reconstructed cell.

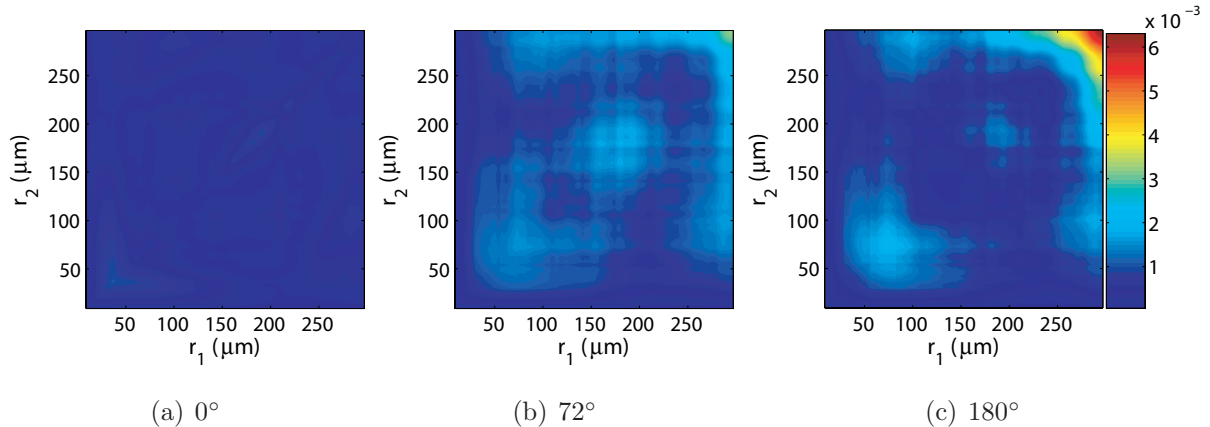


Figure 13: Various samples of $|S_{311}^{orig} - S_{311}^{cell}|$.

Description	Parameter	Value
Minimum separation distance	λ	$2.0 \mu\text{m}$
Maximum refinement distance	ε	$10.0 \mu\text{m}$
Volume fraction before, after	V_i, V_a	0.400, 0.377
Number of tetrahedra	N_e	6,260,115
Number of nodes	N_n	1,102,304

Table 3: Parameters and the mesh information for 40% cell.

value (Table 2). The mesh information can be seen in Table 3 and the periodic mesh can be observed in Figure 14. For the defined minimum separation distance of $2.0 \mu\text{m}$, the total volume fraction of particles was decreased by 5.75%. Note that this variation in volume fraction represents a very small change in particle diameters. Moreover, this difference is added to the small, non-discretized particles to create a homogenized blend. The particle mesh and matrix mesh are shown separately for visualization purposes. Refinements in the mesh can be observed in areas of close particle proximity, resulting in a high mesh quality.

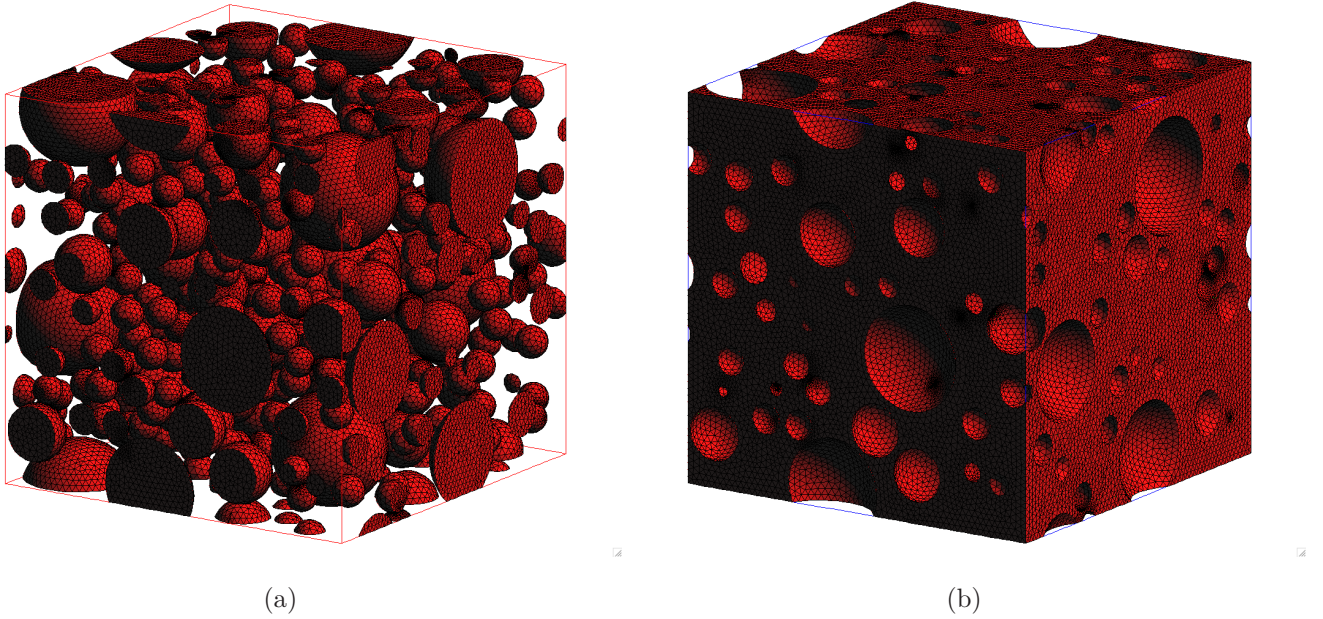


Figure 14: 40% pack: (a) Particle Mesh. (b) Matrix mesh.

5.2 Trimodal Pack with 70% Volume Fraction

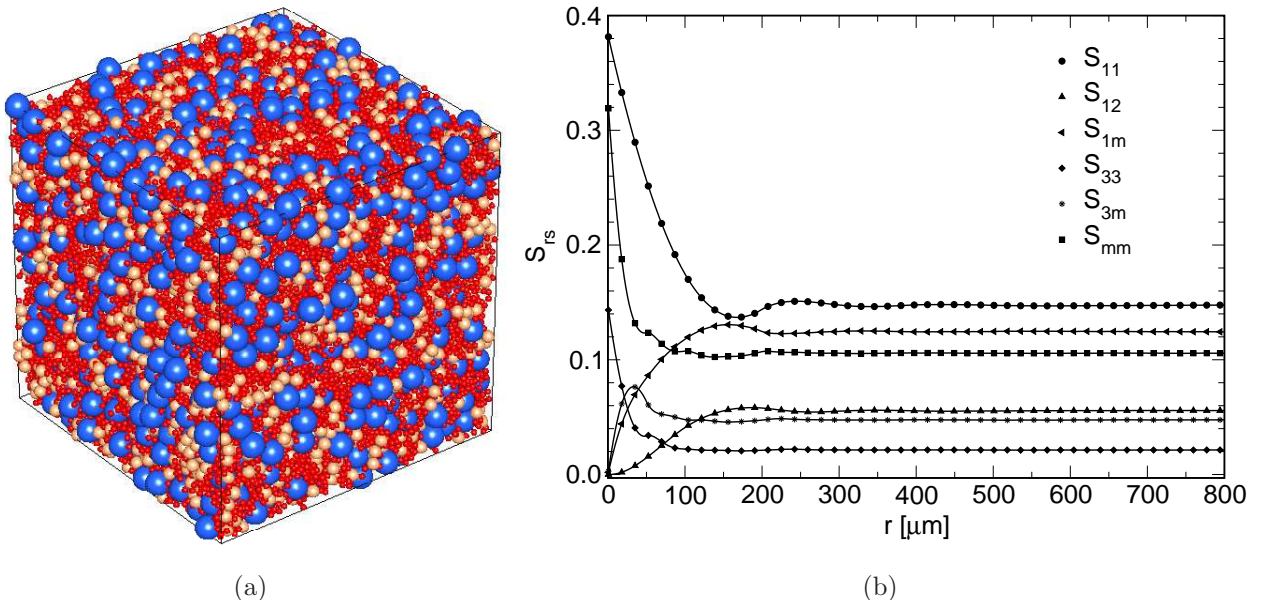


Figure 15: (a) 70% trimodal particle pack containing 50000 particles. (b) Selected two-point probability functions for the 70% pack. Full radius of 1500 μm is not plotted to show the complexity at the origin.

As pointed out in the introduction, materials such as solid propellants are highly packed systems. Thus, we turn our attention to packs with 70% volume fractions to investigate the robustness of our method to reconstruct a highly filled medium. As in the 40% case, 50000

particles are generated in a pack with an edge length $2677.81 \mu\text{m}$. However, for such high volume fraction, the packing code can not reach the theoretical packing density since the inclusions lock in a pack before the theoretical packing density is reached. Therefore, the largest particle with a diameter of $200 \mu\text{m}$ has a volume fraction of 38.96%, the medium particle has a diameter of $100 \mu\text{m}$ with a volume fraction of 14.61%, and the smallest particle has a diameter of $50 \mu\text{m}$ with a volume fraction of 14.61%. This gives the total volume fraction of 68.18%. Selected probability functions together with the pack are shown in Figure 15. Statistical isotropy and homogeneity were again numerically verified.

As can be seen in Figure 15(b), the probability functions are of a more complex shape as compared to the 40% case, and in addition they do not saturate as quickly as before. We select the initial unit cell edge length, H_{in} , by investigating the derivative of the most dominant probability function, S_{11} , along the radial direction (Fig. 16) to accurately account for particle to particle interactions. Figure 16 shows that S_{11} probability function becomes statistically independent for distance $r > 600 \mu\text{m}$. After substituting this initial cell edge length, $H_{in} = 1200 \mu\text{m}$, into Equation (9), an optimal cell dimension is computed as $H = 1199.5 \mu\text{m}$ and the cell volume fraction yields 67.50 %. This is less than 1% error of the total volume fraction of the pack. However, as one can observe, the 70% composite requires twice the length size than the 40% composite. A similar unit cell size has been observed experimentally by Liu [8], for a highly packed plastically bonded explosive PBX 9501, who reported RVE size 1.5 mm or about 15 times the average diameter of the crystals of the material.

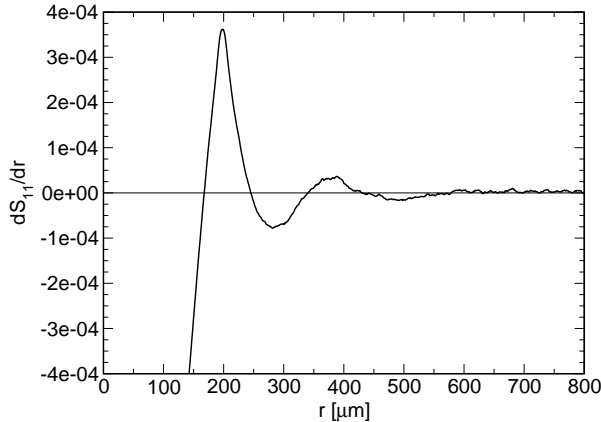


Figure 16: The derivative of the S_{11} probability function with respect to the radial distance, $\frac{dS_{11}}{dr}$.

Due to the complexity of the probability space and in order to test the potential of the reconstruction scheme, we use very fine sampling parameters (number of throws 50000, number of radial points 2000 and number of circumferential rays 20 (see Fig. (2)). This renders the optimization problem very difficult and we use 2048 processors on the Red Storm computer at Sandia National Laboratories, NM. All the AUSA parameters are the same as those reported in section 5.1. We again perform five optimization runs, from which results are reported in

Pack #	Raw Fitness F (Eq. 10)						# of iter.	Overall overlap ($\tilde{\eta}$)		
	Before GA			After GA						
	Min	Mean	Max	Min	Mean	Max				
Run 1	7.828	17.406	28.569	0.511	0.590	0.713	628	0.0000		
Run 2	7.729	17.388	27.838	0.477	0.538	0.746	792	0.0000		
Run 3	7.574	17.171	28.050	0.488	0.600	0.897	1026	0.0000		
Run 4	7.735	17.203	28.450	0.553	0.616	0.762	999	0.0000		
Run 5	7.755	17.147	27.840	0.572	0.663	0.906	874	0.0000		

Table 4: Final objective function values, number of iterations needed for convergence and overall overlap for the 70% pack.

Table 4. The cells have been optimized by about 92% again with no overlap present.

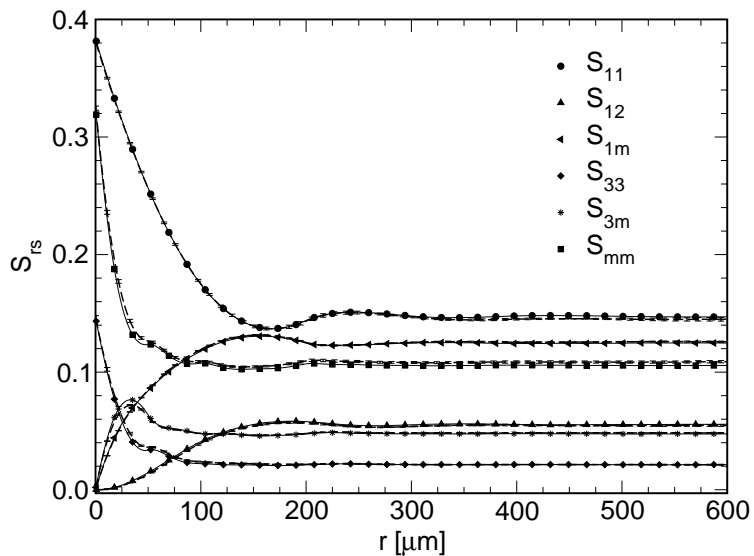


Figure 17: Comparison of the selected two-point probability functions of the original pack (solid line) and the reconstructed PUC (dashed line) for the 70% pack.

Figure 17 shows the comparison of the mean two-point probability functions of the five reconstructed PUCs and the original pack. As in the 40% case, the error bars indicate the standard deviation in the evaluation of the two-point probability functions in the five original packs as well as the numerical error associated with the optimal sampling parameters. However, due to the very high quality of sampling selected for this problem, the standard deviation is very small for all selected probability functions. Very good agreement has been obtained even for this highly packed system.

To compare the pack and the statistically optimal unit cell, we plot them side by side with the same scale in Figure 18. The cell size is approximately one-eighth of the large pack in

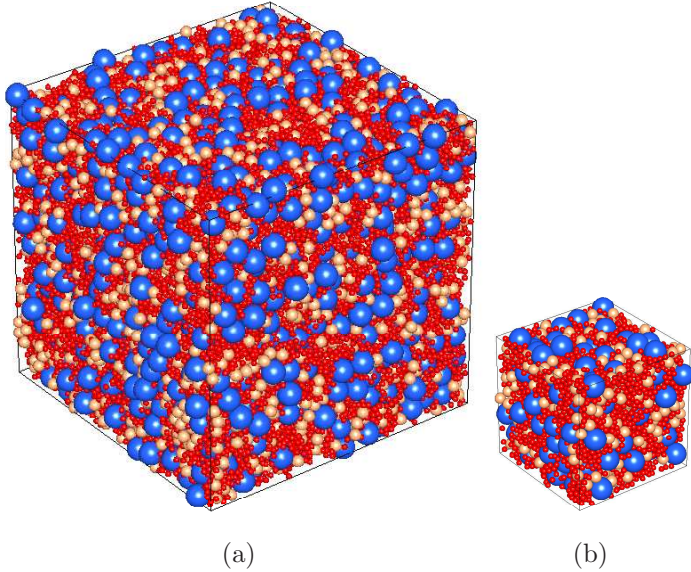


Figure 18: (a) Initial pack consists of 50000 particles. (b) Statistically identical unit cell consists of 4501 particles.

volume, which is a large reduction of the computational space compared to the actual pack.

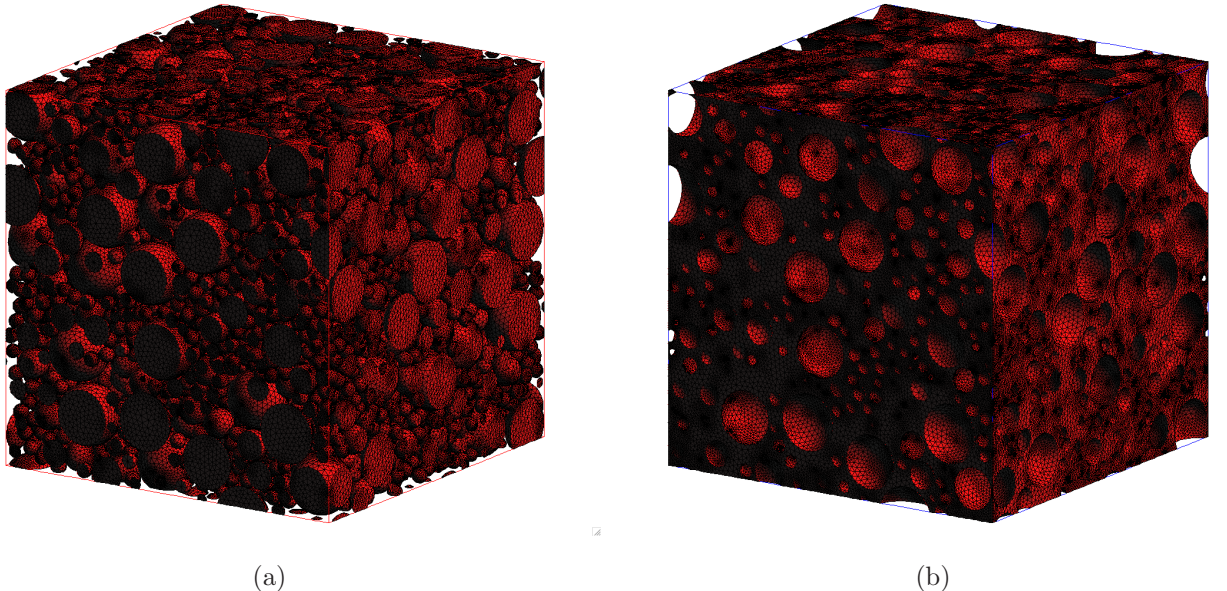


Figure 19: 70% pack: (a) Particle Mesh. (b) Matrix mesh.

The pack discretization is very complex, due to the particle to particle proximity. We use the same mesh control parameters as for the 40% case (Table 3). This leads to the volume fraction reduction by 7.11% (Before discretization, 67.50%. After discretization, 62.70%). Note that a better volume fraction control can be obtained by stringent shrinking parameters. However, this leads to a large mesh density. Removed particle volume is added into a binder and homogenized into a blend. The resulting mesh has 3,232,787 nodes and 18,561,290 tetrahedra elements. High

quality discretization of the statistically optimal cell is shown in Figure 19.

5.3 Parallel Performance

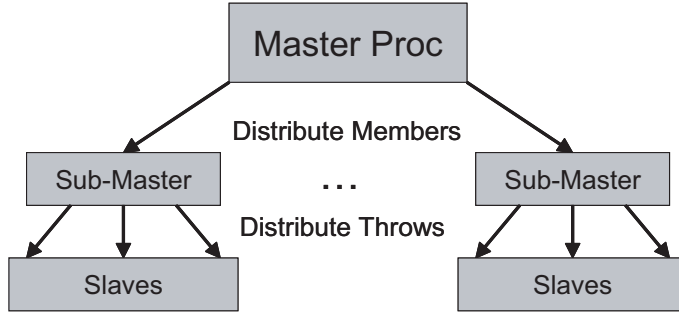


Figure 20: Parallelization of GA.

Due to the independence of statistical sampling, this problem is naturally parallelizable. The only part of the AUSA algorithm that is numerically intensive is the fitness evaluation of members. Taking this into regard, a master-slave parallelization technique, shown in Figure 20, is implemented. The master processor performs all the genetic operations and when fitness evaluations are required, individuals are distributed to slave processors where the computations take place.

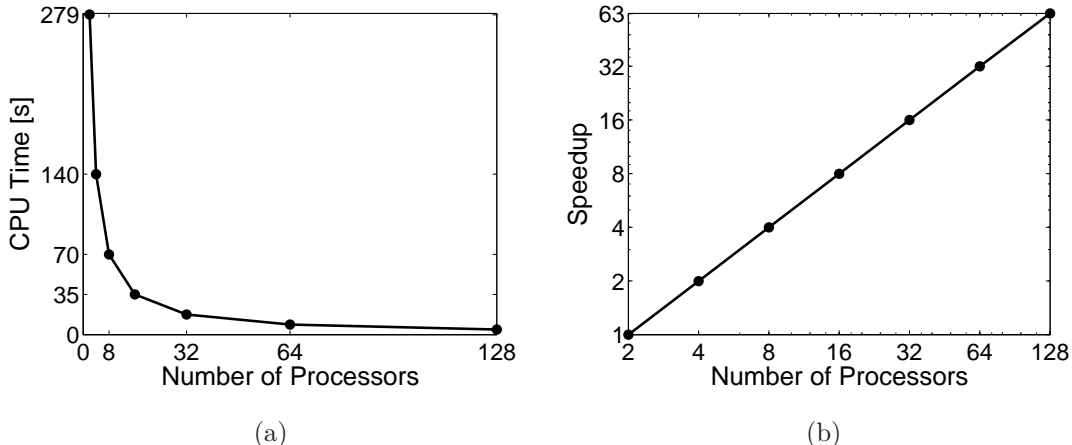


Figure 21: (a) Time for 50000 template throws. (b) Speedup for 50000 template throws.

The master processor first distributes each member to be evaluated to a sub-master, who in turn distributes it to its own slaves. Then, among each subgroup, the number of template throws are divided evenly among the processors. The final probability functions are sent back to the sub-master, who evaluates the fitness and reports it to the master. If the number of processors is less than the number of individuals to be evaluated, the scheme described above is simplified in the fact that there is only one level of parallelization.

In order to test the robustness of our parallelization, the genetic algorithm cycle is run for a total of 50000 template throws on a varying number of processors (40% pack is used for this study). The time and speedup for the runs can be seen in Figure 21. It is observed that the speedup is nearly linear, which is expected for this naturally parallel problem.

6 Conclusions

An efficient and highly parallel procedure to reconstruct a statistically optimal periodic unit cell from a computer generated microstructure has been developed. This procedure consists of finding the statistical descriptors of a random composite, then using stochastic optimization methods to create a PUC with statistics that are similar to those of the original microstructure. It is important to note that the reconstructed periodic unit cells are only representative from a geometrical statistics point of view and that the representativity of the PUC must also account for the physical processes of interest. However, the construction of a geometrically equivalent periodic unit cell is an important first step in describing behavior of complex particulate materials, such as solid propellants.

For the present study, one-, two- and three-point probability functions have been identified as the suitable statistical descriptors. Higher order statistics will allow for more accurate material description once the nonlinear processes are investigated. Such processes are highly influenced, for example, by small particles acting like stress concentrators in between two big particles. Such occurrences can be statistically measured by the third-order probability functions and this information can be used in advanced homogenization schemes.

Computer generated, highly filled, particulate composites have been statistically characterized and optimal unit cells have been reconstructed with a high accuracy. For a highly packed system, unit cell dimensions obtained from our analysis are consistent with those experimentally observed. Novel periodic meshing, based on the master/slave approach, has been extended to three-dimensions and the reconstructed cells of 40% and 70% volume fraction have been successfully discretized for subsequent analysis. The linear scalability of the optimization scheme has been demonstrated.

A natural direction of further research is to extend this procedure to include optimization of three-point probability functions. Another possible future research direction involves extending the genetic algorithm to include optimization of other geometric objects, such as ellipsoids, rhombi, etc. Also, direct reconstruction from tomographic data is of interest.

Acknowledgments

K. Matouš and B.C. Collins would like to gratefully acknowledge the support from ARK/Thiokol (ATK-21316), with J. Thompson and Dr. I. L. Davis serving as program monitors and from the Center for Simulation of Advanced Rockets (CSAR) at the University of Illinois under

the contract number *B523819* by the U.S. Department of Energy as a part of its Advanced Simulation and Computing (ASC) program. D. Rypl would like to gratefully acknowledge the Ministry of Education of Czech Republic in the framework of the project No. MSM 6840770003. The authors also thank Michael Campbell for running the reconstruction code on Red Storm computer located at Sandia National Laboratories, NM. Moreover, the authors gratefully acknowledge the use of the Turing cluster maintained and operated by the Computational Science and Engineering Program at the University of Illinois.

References

- [1] Hill, R., Elastic properties of reinforced solids - some theoretical principles. *Journal of the Mechanics and Physics of Solids*, 11:357–372, 1963.
- [2] Hashin, Z. and Shtrikman, S., On some variational principles in anisotropic and non-homogeneous elasticity. *Journal of the Mechanics and Physics of Solids*, 10:335–342, 1962.
- [3] Collins, B., Maggi, F., Matouš, K., Jackson, T. L., Buckmaster, J., Using Tomography to Characterize Heterogeneous Propellants, *46th AIAA Aerospace Sciences Meeting and Exhibit*, Paper No: AIAA 2008-941, Reno, NV, 2008.
- [4] Kochevets, S.V., Buckmaster, J., Jackson, T.L., Hegab, A., Random packs and their use in the modeling of heterogeneous solid propellant combustion. *Journal of Propulsion and Power*, 17(4):883–891, 2001.
- [5] Matouš, K. and Geubelle, P. H., Multiscale modelling of particle debonding in reinforced elastomers subjected to finite deformations. *Int. J. Numer. Meth. Engng*, 65:190–223, 2006.
- [6] Povirk, G. L. Incorporation of microstructural information into materials. *Acta Metallurgical Materials*, 43:3199-3206, 1995.
- [7] Swaminathan, S., Ghosh, S., Statistically Equivalent Representative Volume Elements for Unidirectional Composite Microstructures: Part II - With Interfacial Debonding. *Journal of Composite Materials*, 40(7): 605–621, 2006.
- [8] Liu, C., On the Minimum Size of Representative Volume Element: An Experimental Investigation. *Experimental Mechanics*, 45(3):238-243, 2005.
- [9] Matouš, K., Inglis, H.M., Gu, X., Rypl, D., Jackson, T.L., Geubelle, P.H., Multiscale modeling of solid propellants: From particle packing to failure. *Composites Science and Technology*, 67:1694–1708, 2007.
- [10] Fish J, Chen W. RVE Based Multilevel Method For Periodic Heterogeneous Media With Strong Scale Mixing. *Journal of Applied Mathematics*, 46:87–106, 2003.
- [11] Rypl D. Sequential and Parallel Generation of Unstructured 3D Meshes, PhD thesis. Prague: CTU Reports, No. 2, Vol. 3, Czech Technical University, 1998. *T3D* page; <http://ksm.fsv.cvut.cz/~dr/t3d.html>

- [12] Lions JL, Some Methode in the Mathematical Analysis of systems and their Control. New York: Gordon and Breach, Science Publisher, Inc., 1981.
- [13] Torquato, S., *Random Heterogeneous Media*. Springer Publishers, New York, 1st edition, 2002.
- [14] Torquato, S. and Stell, G, Microstructure of two-phase random media. i. the n-point probability functions. *Journal of Chemical Physics*, 77:2071-2077, 1982.
- [15] Corson, P. B., Correlation functions for predicting properties of heterogeneous materials. i. experimental measurement of spatial correlation functions in multiphase solids. *Journal of Applied Physics*, 45(7): 3159-3164, 1974.
- [16] Smith, P. and Torquato, S. Computer simulation results for the two-point probability function of composite media *Journal of Computational Physics* 76:176-191, 1988.
- [17] Yeong, C. L. Y. and Torquato, S. Reconstructing random media. *Physical Review E*, 57(1):495–506, 1998.
- [18] Bochenek, B. and Pyrz, R. Reconstruction of random microstructures—a stochastic optimization problem. *Computational Materials Science*, 31:93–112, 2004.
- [19] Sundararaghavan, V. and Zabaras, N. Classification and reconstruction of three-dimensional microstructures using support vector machines. *Computational Materials Science*, 32:223–239, 2005.
- [20] Kumar, N. C., Matouš, K., Geubelle, P. H., Reconstruction of periodic unit cells of multimodal random particulate composites using genetic algorithms, *Computational Materials Science.*, 42, 352–367 (2008).
- [21] Matouš, K., Lepš, M., Zeman, J., Šejnoha, M., Applying genetic algorithms to selected topics commonly encountered in engineering practice. *Computer Methods in Applied Mechanics and Engineering*, 190:1629–1650, 2000.
- [22] Zeman J, Šejnoha M. Numerical evaluation of effective elastic properties of graphite fiber tow impregnated by polymer matrix. *J. of the Mechanics and Physics of Solids* 2001;49:69–90.
- [23] Talbot, D.R.S. and Willis, J.R., Variational principles for inhomogeneous nonlinear media. *IMA J. Appl. Math.*, 35:39–54, 1985.
- [24] Knott, G.M., Jackson, T.L., Buckmaster, J., The random packing of heterogeneous propellants. *AIAA Journal*, 39(4):678–686, 2000.
- [25] Beran, M. J., *Statistical Continuum Theories*. Interscience Publishers, 1968.
- [26] Matouš, K. and Dvorak, J.G., Optimization of electromagnetic absorption in laminated composite plates. *IEEE Transactions on Magnetics*, 39(3):1827–1835, 2003.
- [27] Goldberg, D., *Genetic Algorithms in Search, Optimization and Machine Learning*. Addison-Wesley, 1989.

- [28] Cignoni P., Montani C., Scopigno R., *DeWall: A fast divide and conquer Delaunay triangulation algorithm in E^d* . Computer-Aided Design, Volume 30, Number 5, April 1998 , pages 333-341(9)
- [29] Hughes, T.J.R., *The Finite Element Method: Linear Static and Dynamic Finite Element Analysis*. Dover, 2000.
- [30] Demmel, J.W., Eisenstat, S.C., Gilbert, J.R., Li, X.S., Liu, J.W.H., A supernodal approach to sparse partial pivoting. *SIAM J. Matrix Analysis and Applications*, 20(3):720–755, 1999.
- [31] Wentorf R, Collar R, Shephard MS, Fish J. Automated modeling for complex woven mesostructures. *Computer Methods in Applied Mechanics and Engineering*. 1999;172(1-4):273-291.
- [32] Bittnar Z, Rypl D. Direct Triangulation of 3D Surfaces Using Advancing Front Technique. In: Proceedings of the Second ECCOMAS Conference on Numerical Methods in Engineering, J. Wiley & Sons, Paris, France, 1996;86–90.
- [33] B.C. Collins. Reconstruction of Statistically Optimal Periodic Unit Cells of Multimodal Particulate Composites, M.S. Thesis, University of Illinois at Urbana-Champaign, IL, 2008.